PNAS
www.pnas.org

Supplementary Information for

Modular reconfiguration of an auditory-control brain network supports adaptive listening behavior

Mohsen Alavash, Sarah Tune, Jonas Obleser

Author correspondence: Mohsen Alavash, Jonas Obleser
Email: mohsen.alavash@uni-luebeck.de; jonas.obleser@uni-luebeck.de

This PDF file includes:

Supplementary text
Figs. S1 to S6
Tables S1 to S4
References for SI reference citations

Experimental paradigm

In our linguistic variant of the classic Posner paradigm, participants listened to two competing, dichotically presented sentences and were probed on the sentence-final word in one of the two sentences (Fig. 2A). Crucially, sentence presentation was preceded by two different visual cues that informed participants about the to-be-probed side (spatial cue) and the semantic category of the two sentence-final nouns (semantic cue). Each cue could be informative or uninformative and the combination of individual cue levels followed a 2x2 design and varied on a trial-by-trial level.

Each trial started with the visual presentation of a fixation cross in the middle of the screen (jittered duration, mean 1.5 s, range 0.5–3.5 s) followed by the presentation of the spatial cue in the form of a circle segmented equally into two lateral halves. An informative cue provided information about the side (left ear vs. right ear) of the to-be-probed sentence-final word depending on which half of the circle (left or right) was black. In contrast, an uninformative cue was grey in both halves, and thus did not provide information about the side of the to-be-probed sentence-final word. As such, while the informative spatial cue invoked selective attention, the uninformative spatial cue invoked divided attention. The spatial cue was presented for one second.

After 500 ms of a blank screen, the trial was continued by the visual presentation of the semantic cue in the form of a single word. This word specified a general (natural vs. man-made) or one of 20 specific semantic categories. The semantic category cue applied to both sentence-final nouns, and allowed the generation of semantic prediction about the upcoming sentence-final noun. The semantic cue was presented for one second. The two cues were presented in a fixed order. Following a second jittered period, the two sentences were presented dichotically along with a fixation cross displayed in the middle of the screen. Finally, after a jittered retention period, a visual response array appeared on the left or right side of the scene, presenting four word choices. Participants had four seconds to identify the final word of the probed ear, indicated by the side at which the response array was presented (L/R). Among the four alternative were the two actually presented nouns as well as two distractor nouns from the same cued semantic category.

Before the fMRI measurement, participants completed a short practice session of the listening task outside the scanner room to make sure they understood the task. Next, participants were placed in the scanner and went through a short sound volume adjustment to ensure balanced hearing between left and right ears at a comfortable level.

On a separate day before the imaging session, the older participants (>35 yrs) underwent a general screening procedure, detailed audiometry, and a battery of cognitive tests and personality profiling (see ref. [7], main text, for details). Only participants with normal hearing or age-adequate mild-to-moderate hearing loss were invited for the imaging session.

Sentence materials and recordings

Speech stimuli consisted of 240 pairs of short German declarative sentences of fixed syntactic structure. All sentences were five words long. They always began with a first name, followed by sequence of a transitive verb, a temporal adverb, a case- and gender-ambiguous numeral and finally a plural noun (e.g., *"Anna zeichnete gestern drei Stühle"*; literal translation *"Anna drew yesterday three chairs"*). The number of syllables at each sentence position was held constant to control for overall sentence length. Different sentence contexts (i.e., consisting of the first four words) were constructed by filling each position with one of ten possible alternatives. The ten possible words for each position were chosen in a way that they would yield equally plausible but unpredictable combinations with the other context words, and importantly, with each of the 120 different sentence-final nouns. Of all theoretically possible sentence permutations, we created 240 sentence pairs that differed at every word position. The task-relevant, sentence-final nouns belonged to two overarching general semantic categories: natural and man-made. In each of the two general categories there were ten specific subcategories (e.g., pets, fruits, vegetables in the natural, or instruments, furniture, tools in the man-made category) that each consisted of six highly representative members derived from a pre-experiment questionnaire study. Each noun was used four times across the final pool of sentence pairs, but always combined with different sentence contexts.

A trained female speaker of standard German recorded the individual sentences in a sound-attenuated recording chamber (sampling rate, 44 kHz). Root mean square (RMS) intensity (–26 dB Full Scale, FS) was equalized across all individual sentences. When combining the sentence recordings per pair, we

temporally aligned them by the onset of the two sentence-final nouns to ensure their simultaneous presentation. Sentence presentation was masked by continuous speech-shaped noise at a signal-to-noise-ration of 0 dB. Noise onset (with a 50 ms linear onset ramp) preceded sentence onset by 200 ms. Final speech stimuli had an average length of 2512 ms (range: 2183 to 2963 ms). All participants listened to the same 240 sentence pairs but in subject-specific randomized order. In addition, across participants we balanced the assignment of sentences to the right and left ear, respectively.

MRI data acquisition

Functional MRI data were collected by means of a Siemens MAGNETOM Skyra 3T scanner using a 64-channel head/neck coil and an echo-planar image (EPI) sequence [repetition time (TR) =1000 ms; echo time (TE) =25 ms; flip angle (FA) =60°; acquisition matrix =64×64; field of view (FOV) =192 mm × 192 mm; voxel size =3×3×3 mm; slice spacing =3 mm]. Each image volume had 36 oblique axial slices parallel to the anterior commissure-posterior commissure (AC-PC) line, and was acquired with an acceleration factor of 2. Structural images were collected using a magnetization prepared rapid gradient echo (MP-RAGE) sequence [TR =1900 ms; TE =2.44 ms; FA =9°; 1-mm isotropic voxel; 192 sagittal slices]. Although the acoustic noise associated with continuous imaging makes an auditory task more difficult, we used the same sequences for resting state and task with a comparable background scanner noise, which would cancel out in the task versus rest contrast.

Definition of graph-theoretical network metrics

***Global network efficiency*.** In a graph-theoretical sense, global network efficiency is a measure of information processing capacity of a network. For a given graph G comprised of N nodes, global efficiency E_{global} summarizes the capacity of the network for parallel processing across distributed nodes. This metric is estimated by the inverse of the harmonic mean of the shortest path lengths (i.e. the smallest number of intervening connections) between each pair of nodes $L_{i,j}$:

$$E_{global} = \frac{1}{N(N-1)} \sum_{i \neq j \in G} \frac{1}{L_{i,j}} \qquad \text{(Eq.1)}$$

An efficient network is characterized by having a short average minimum-path between all pairs of nodes. Such a network is considered to have high efficiency in parallel (or global) information processing [1].

Local network efficiency. By slightly zooming out from a given node within a graph, the nearest neighbors of that node which are directly connected to each other form a cluster. This local integration can be quantified based on the local efficiency of node , $E_{local(i)}$, which is mathematically equivalent to global efficiency (Eq.1) but is computed on the immediate neighborhood of node i. On the whole-brain level, mean local efficiency can be quantified by averaging local efficiency across all nodes:

$$E_{local} = \frac{1}{N} \sum_{i \in G} E_{local(i)} \qquad \text{(Eq.2)}$$

***Network modularity*.** Modularity describes the decomposability of a network into non-overlapping sub-networks, characterized by having relatively dense intra-connections and relatively sparse inter-connections. Rather than an exact computation, modularity of a given network is estimated using optimization algorithms [2, 3]. The extent to which a network partition exhibits a modular organization is measured by a quality function, the so-called *modularity index* (Q). We used a common modularity index originally proposed in [4], and employed its implementation in the Brain Connectivity Toolbox [5] which is based on the modularity maximization algorithm known as Louvain [6]. The modularity index is defined as:

$$Q = \frac{1}{2W} \sum_{i,j} \left[A_{i,j} - \gamma \frac{k_i k_j}{2W} \right] \delta(c_i, c_j) \qquad \text{(Eq.3)}$$

Q ranges between –1 and 1. In Eq. 3, $A_{i,j}$ represents the weight (zero or one if binary) of the links between node i and j, k_i=$\sum_j A_{i,j}$ is the sum of the weights of the links connected to node i, and c_i is the community or module to which node i belongs. The δ-function $\delta(u,v)$ is 1 if $u = v$ and 0 otherwise, and $W = \frac{1}{2} \sum_{i,j} A_{i,j}$. Similar to previous work [7-9], the structural resolution parameter γ [10, 11] was set to unity for simplicity. The maximization of the modularity index Q gives a partition of the network into modules such that the total connection weight within modules is as large as possible, relative to a commonly used null model whose total within-module connection weights follows $\frac{k_i k_j}{2W}$. Thus, a “good"

partition with Q closer to unity gives network modules with many connections within and only few connections between them; in contrast, a “bad" partition with Q closer to zero gives network modules with no more intra-module connections than expected at random [12]. Thus, higher Q reflects higher functional segregation on the intermediate level of network topology [5, 13]. Due to stochastic initialization of the greedy optimization, the module detection algorithm was applied 100 times for each brain graph, and the highest Q value obtained was used as the modularity index in the subsequent statistical analyses.

Consensus modularity. Repetition of the module detection algorithm leads to multiple possible high-modularity partitions that maximize Q for a given network, resulting in module membership assignments that vary across runs of the algorithm [12, 14, 15]. In order to account for this variability, we used the consensus approach proposed in [16] whereby an agreement matrix is calculated, representing the probability of each node pair to be assigned to the same module across iterations. Finally, the agreement matrix was subjected to an independent module detection, resulting in an individual-level (or group-representative when the input was group-average connectivity matrix) high-modularity partition. In this step, the resolution parameter τ was set to 0.75, representing the level at which the agreement matrix was thresholded before being subjected to the final module detection. Similar results were obtained when τ =0.5 or τ =1. The modularity detection was implemented with no prior community affiliation input, hence in a purely data-driven fashion.

Within– and between–module connectivity. Based on the results obtained from consensus module detection, mean within- (between-) module connectivity was estimated as the sum of connection weights falling within (between) modules, normalized by maximum number of possible within- (between) module connections (Garcia et al., 2018). In contrast to the overall mean functional connectivity, this is done by focusing on only the connections that fall within or between modules, respectively:

$$FC_{m_1,m_2} = \frac{\sum_{i \in m1, j \in m2} w_{i,j}}{N_{m1} N_{m2}} \qquad \text{(Eq.4)}$$

In Eg.4, $w_{i,j}$ represent the connection weight between node i of module m_1 and node j of module m_2, and N is the number of nodes. When $m_1 = m_2$, the result gives the functional connectivity within a single module. More precisely, in the case of within-module connectivity per participant, for each module we calculated the sum of connection weights (i.e., correlations) for each pair of nodes that are grouped within that module. This sum is then normalized by dividing the result by the total number of connections in the same module. Finally, to get a whole-brain estimate of within-module connectivity, the scores are averaged across all modules. In the case of between-module connectivity, the summation and normalization is done across all pairs of modules, and the results are then averaged.

***Group-level modularity partition*.** Based on the results obtained from graph-theoretical consensus community detection (see above), group-level functional connectivity per resting state and listening task was computed by first averaging unthresholded (raw) connectivity matrices across all participants, and then including the top 10% of the connections in the graph according to the rank of their correlation strengths[17, 18]. To obtain group-level modularity partition, the graph-theoretical consensus community detection algorithm was applied to the sparse group-level connectivity matrix (identical to [19]). Similar to [20], modules with fewer than five nodes were removed, and the result was used for visualization (main text: *Data visualization*). To functionally identify the network modules, we used the labels assigned to each cortical node as in [20].

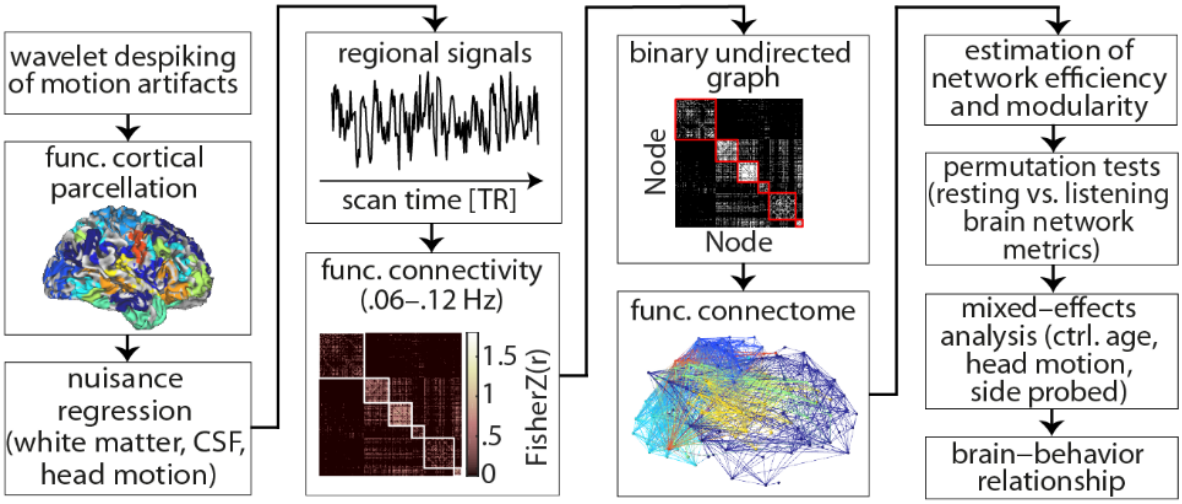

Fig. S1. Analysis steps through which artifact-clean regional BOLD signals were averaged per cortical parcel. The results were used to construct graph-theoretical models of the functional connectome during resting state and the listening task, to ultimately investigate brain-behavior relationship using (generalized) linear mixed-effects analysis.

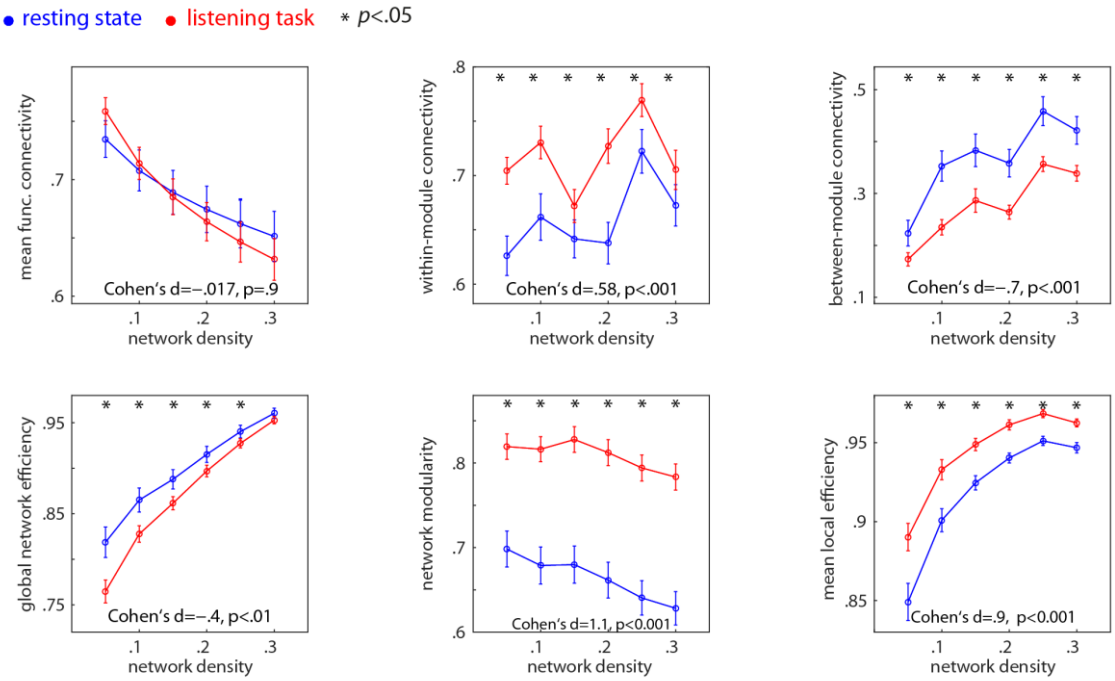

Fig. S2. The effect of graph thresholding on the whole–brain results. For the analysis reported in the main text, the choice of the graph threshold (10%) was guided by previous studies showing that behavioral correlates of brain networks are found within a range of low thresholds, usually 5%–30% of connection density [7, 8, 21, 22]. To directly investigate this range in the present study, we examined the effect of graph thresholding using cost-integration approach [17]. We found that higher functional segregation of the whole–brain network during the listening task relative to resting state was not specific to a certain network density. Data in each plot show max–normalized values per density (error bar: SEM). P-values within each plot are based on pared permutation tests applied to the data averaged over the whole range of network density (cost-integration).

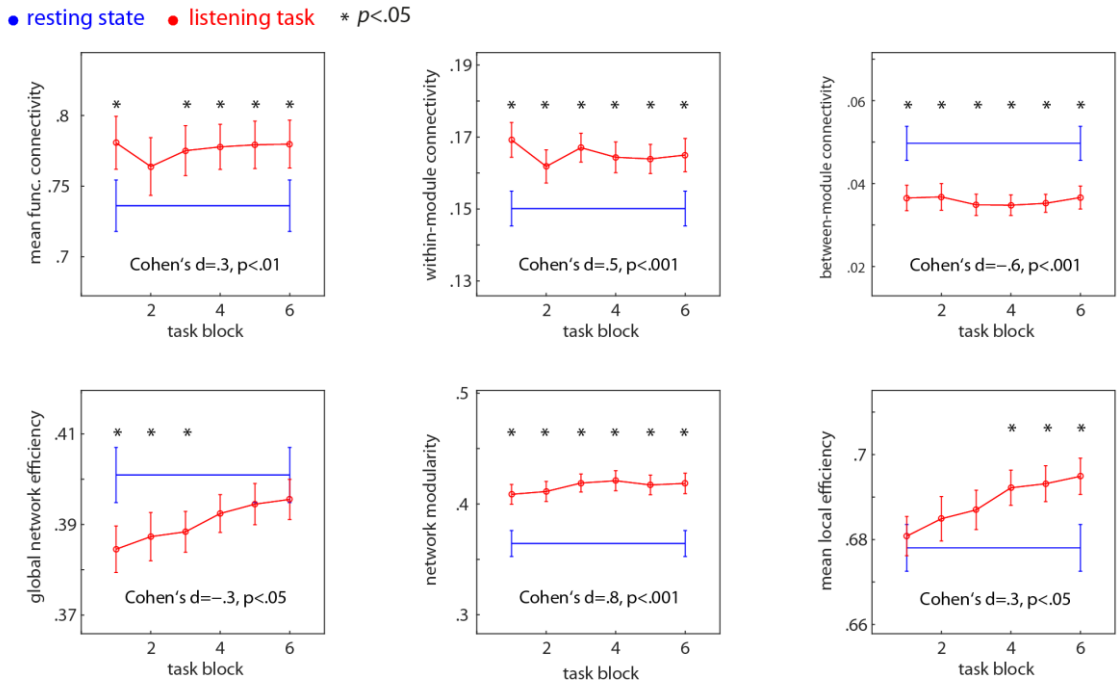

Fig. S3. Consistency of higher functional segregation of the whole-brain network during six blocks of the listening task relative to resting state. The comparisons at each block is based on permutation tests for paired samples (error bars: SEM). Cohen's d and P-values within each plot are based on pared permutation tests applied to the task data averaged over the six blocks as compared to resting state.

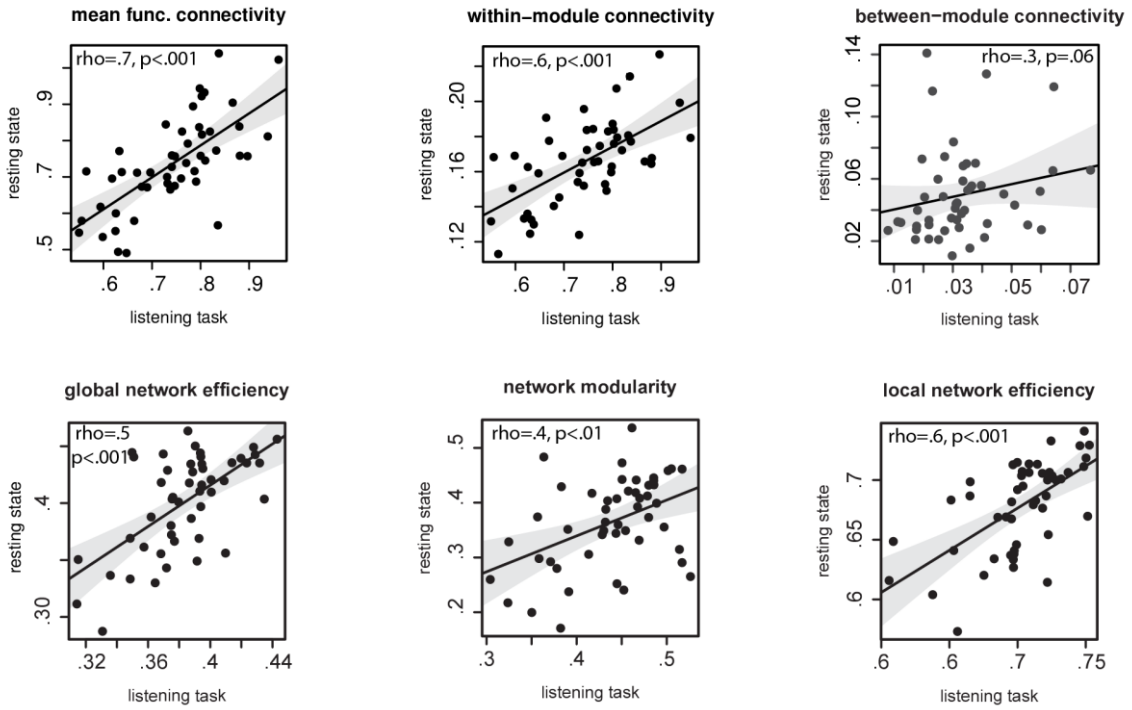

Fig. S4. Correlation between brain network measures across resting state and the listening task. The significance of the Spearman's correlations (rho) was tested using permutation tests with 10,000 randomizations. Shaded area shows two-sided parametric 95% CI.

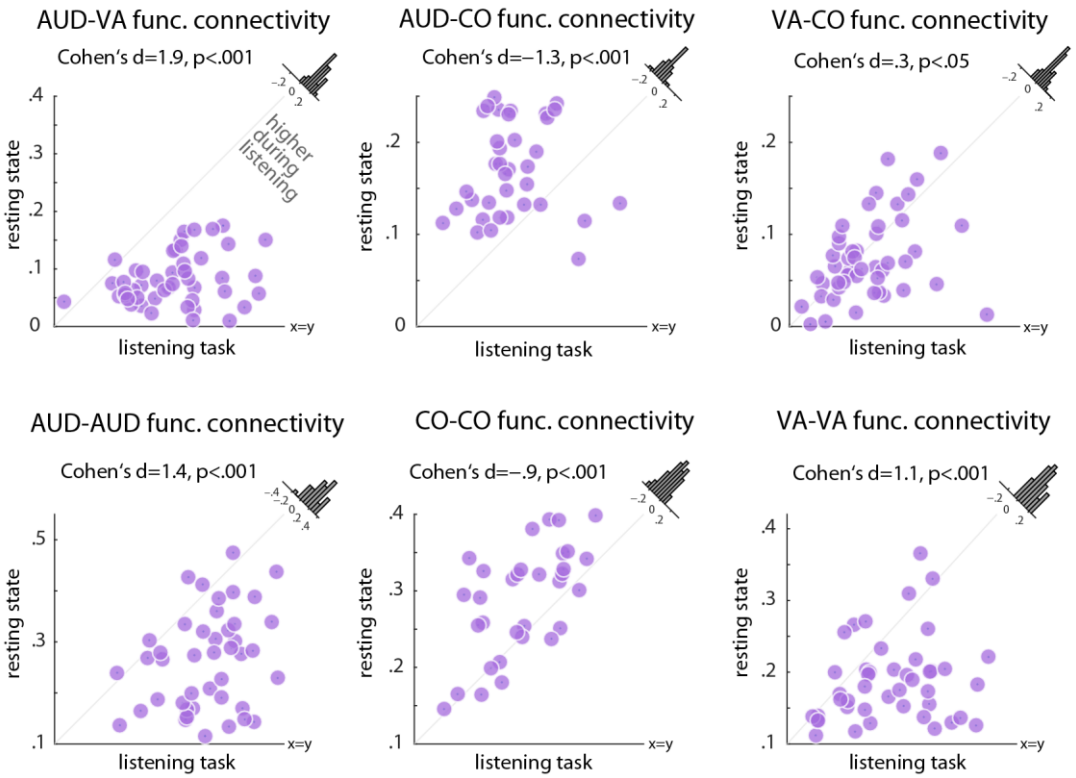

Fig. S5. Alterations in functional connectivity within the auditory-control network during the listening task relative to resting state. Mean functional connectivity was significantly increased within the auditory nodes (AUD), ventral attention nodes (VA), as well as between auditory and ventral attention nodes. Conversely, mean functional connectivity was significantly decreased within cingulo-opercular (CO) nodes as well as between auditory and cingulo-opercular nodes. Histograms show the distribution of the change (task minus rest) of mean functional connectivity across all 49 participants.

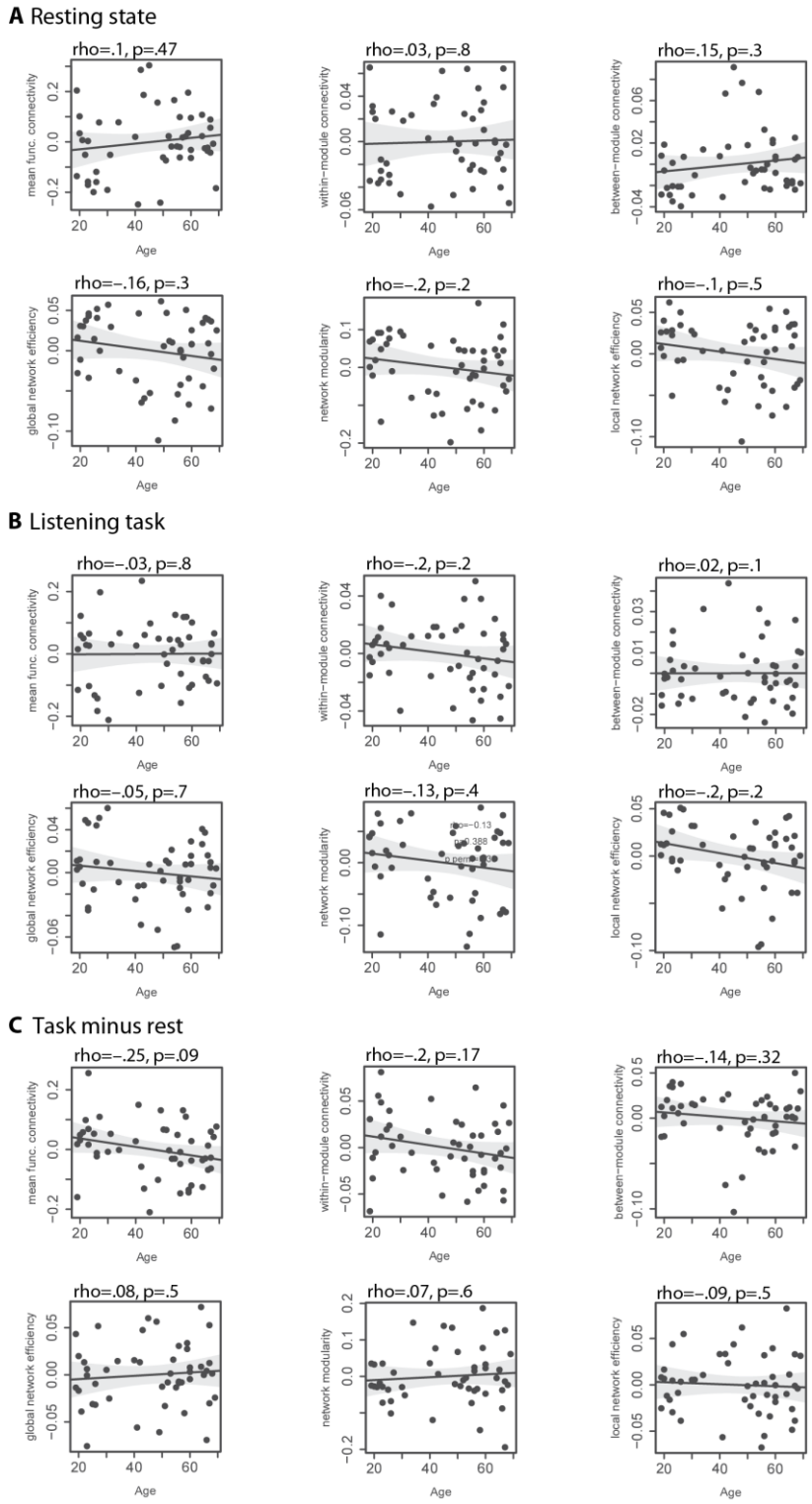

Fig. S6. Correlation between brain network measures and age. Root mean square (RMS) of frame-wise displacement, as a measure of head motion, was regressed out from the brain network measures prior to testing the correlations.The significance of the Spearman's correlations (rho) was tested using permutation tests with 10,000 randomizations. Shaded area shows two-sided parametric 95% CI.

Table S1. Linear mixed-effects models predicting individuals' listening performance. The corresponding models were constructed to investigate prediction of **(A)** single-trial binary accuracy (1/0) in word identification or **(B)** speed of word identification (1/RT) from the listening cues (i.e., spatial cue and semantic cue) and change in modularity of the whole-brain network (DiffModularity). Significant effects are shown in blue. The main effects of the listening cues are plotted in Figure 2B (main text). OR: Odds ratio; β: slope parameter estimate; σ^2: within-group variance; τ_{00}: between-group variance; ρ_{01}: random-slope-intercept-correlation.

A Prediction of accuracy

	OR	CI	p
Fixed Parts			
(Intercept)	5.41	4.50 – 6.51	<.001
SpatialCueSelective	2.10	1.90 – 2.32	<.001
SemanticCueSpecific	1.12	1.01 – 1.23	.026
ProbeRight	1.22	0.98 – 1.52	.071
Age	0.63	0.52 – 0.76	<.001
DiffModularity (task minus rest)	1.09	0.91 – 1.31	.357
SpatialCueSelective:DiffModularity	1.14	1.03 – 1.25	.009
ProbeRight:DiffModularity	0.82	0.66 – 1.01	.060
Random Parts			
$\tau_{00,\,Subject}$		0.393	
ρ_{01}		–0.003	
$N_{Subject}$		49	
$ICC_{Subject}$		0.107	
Observations		11760	
Deviance		9965.418	

B Prediction of response speed

	β	CI	p
Fixed Parts			
(Intercept)	0.66	0.64 – 0.69	<.001
SpatialCueSelective	0.11	0.10 – 0.13	<.001
SemanticCueSpecific	0.03	0.02 – 0.04	<.001
ProbeRight	0.02	0.01 – 0.03	.004
Age	-0.03	-0.05 – -0.02	<.001
DiffModularity (task minus rest)	0.01	-0.02 – 0.04	.428
SpatialCueSelective:DiffModularity	0.01	-0.00 – 0.03	.144
ProbeRight:DiffModularity	-0.02	-0.03 – -0.01	<.001
Random Parts			
σ^2		0.042	
$\tau_{00,\,Subject}$		0.009	
ρ_{01}		0.890	
$N_{Subject}$		49	
$ICC_{Subject}$		0.171	
Observations		9524	
R^2 / Ω_0^2		.247 / .247	

Table S2. Linear mixed-effects models predicting individuals' listening performance from modularity of the whole-brain resting state or task network as separate predictors. The corresponding models were constructed to investigate prediction of **(A)** single-trial binary accuracy (1/0) in word identification or **(B)** speed of word identification (1/RT) from the listening cues (i.e., spatial cue and semantic cue) and modularity derived from the whole-brain resting-state (Rest) or listening-task (Task) network (i.e., two separate regressors). Significant effects are shown in blue. *OR*: Odds ratio; β: slope parameter estimate; σ^2: within-group variance; τ_{00}: between-group variance; ρ_{01}: random-slope-intercept-correlation.

A Prediction of accuracy

	OR	CI	p
Fixed Parts			
(Intercept)	5.41	4.50 – 6.50	<.001
SpatialCueSelective	2.09	1.89 – 2.31	<.001
SemanticCueSpecific	1.12	1.01 – 1.23	.026
ProbeRight	1.22	0.98 – 1.51	.070
Age	0.63	0.52 – 0.76	<.001
RestModularity	0.93	0.76 – 1.15	.505
TaskModularity	1.08	0.88 – 1.33	.449
ProbeRight:TaskModularity	0.80	0.63 – 1.01	.062
ProbeRight:RestModularity	1.21	0.96 – 1.54	.109
Random Parts			
$\tau_{00, Subject}$		0.393	
ρ_{01}		-0.002	
$N_{Subject}$		49	
$ICC_{Subject}$		0.107	
Observations		11760	
Deviance		9972.266	

B Prediction of response speed

	β	CI	p
Fixed Parts			
(Intercept)	0.66	0.64 – 0.69	<.001
SpatialCueSelective	0.11	0.10 – 0.13	<.001
SemanticCueSpecific	0.03	0.02 – 0.04	<.001
ProbeRight	0.02	0.01 – 0.03	.004
Age	-0.03	-0.05 – -0.02	<.001
RestModularity	-0.02	-0.04 – 0.01	.279
TaskModularity	-0.01	-0.03 – 0.02	.594
SpatialCueSelective:RestModularity	-0.01	-0.03 – 0.00	.057
ProbeRight:TaskModularity	-0.02	-0.04 – -0.01	.001
ProbeRight:RestModularity	0.02	0.01 – 0.04	.001
Random Parts			
σ^2		0.042	
$\tau_{00, Subject}$		0.009	
ρ_{01}		0.882	
$N_{Subject}$		49	
$ICC_{Subject}$		0.169	
Observations		9524	
R^2 / Ω_0^2		.247 / .247	

Table S3. Linear mixed-effects models predicting individuals' listening performance from change in modularity of the auditory–control network. The corresponding models were constructed to investigate prediction of **(A)** single-trial binary accuracy (1/0) in word identification or **(B)** speed of word identification (1/RT) from the listening cues (i.e., spatial cue and semantic cue) and change in modularity derived from the fronto-temporal auditory-control network (DiffModularity). Significant effects are shown in blue. The interactions between the spatial cue and change in modularity of the auditory-control network are plotted in Figure 6B/C. OR: Odds ratio; β: slope parameter estimate; σ^2: within-group variance; τ_{00}: between-group-variance; ρ_{01}: random-slope-intercept-correlation.

A Prediction of accuracy

	OR	CI	p
Fixed Parts			
(Intercept)	5.31	4.34 – 6.48	<.001
SpatialCueSelective	2.13	1.92 – 2.36	<.001
SemanticCueSpecific	1.12	1.01 – 1.23	.026
ProbeRight	1.19	0.92 – 1.54	.180
Age	0.66	0.55 – 0.78	<.001
DiffModularity (task minus rest)	1.30	1.09 – 1.54	.003
SessOrderSessionTwo	0.92	0.61 – 1.38	.680
SpatialCueSelective:DiffModularity	1.12	1.02 – 1.23	.023
ProbeRight:SessOrderSessionTwo	0.92	0.55 – 1.53	.734
Random Parts			
$\tau_{00,\,Subject}$		0.336	
ρ_{01}		-0.081	
$N_{Subject}$		49	
$ICC_{Subject}$		0.093	
Observations		11760	
Deviance		9967.808	

B Prediction of response speed

	β	CI	p
Fixed Parts			
(Intercept)	0.66	0.64 – 0.69	<.001
SpatialCueSelective	0.11	0.10 – 0.13	<.001
SemanticCueSpecific	0.03	0.02 – 0.04	<.001
ProbeRight	0.02	0.00 – 0.03	.009
Age	-0.03	-0.05 – -0.01	<.001
DiffModularity (task minus rest)	0.03	0.01 – 0.06	.005
SpatialCueSelective:DiffModularity	0.02	0.00 – 0.03	.019
Random Parts			
σ^2		0.042	
$\tau_{00,\,Subject}$		0.008	
ρ_{01}		0.870	
$N_{Subject}$		49	
$ICC_{Subject}$		0.153	
Observations		9524	
R^2 / Ω_0^2		.247 / .247	

Table S4. Linear mixed-effects models predicting individuals' listening performance from modularity of the auditory-control network during resting state or task as separate predictors. The corresponding models were constructed to investigate prediction of **(A)** single–trial binary accuracy (1/0) in word identification or **(B)** speed of word identification (1/RT) from the listening cues (i.e., spatial cue and semantic cue) and modularity derived from the auditory-control network under resting-state (Rest) or listening challenge (Task). Significant effects are shown in blue. *OR*: Odds ratio; β: slope parameter estimate. *OR*: Odds ratio; β: slope parameter estimate; σ^2: within-group variance; τ_{00}: between-group-variance; ρ_{01}: random-slope-intercept-correlation.

A Prediction of accuracy

	OR	CI	p
Fixed Parts			
(Intercept)	5.31	4.40 – 6.41	<.001
SpatialCueSelective	2.09	1.89 – 2.31	<.001
SemanticCueSpecific	1.12	1.01 – 1.23	.026
ProbeRight	1.19	0.92 – 1.54	.178
Age	0.70	0.59 – 0.83	<.001
TaskModularity	1.40	1.18 – 1.65	<.001
SessOrderSessionTwo	0.94	0.64 – 1.37	.749
ProbeRight:SessOrderSessionTwo	0.91	0.55 – 1.52	.727
Random Parts			
$\tau_{00, Subject}$		0.295	
ρ_{01}		-0.070	
$N_{Subject}$		49	
$ICC_{Subject}$		0.082	
Observations		11760	
Deviance		9973.492	

B Prediction of response speed

	β	CI	p
Fixed Parts			
(Intercept)	0.66	0.64 – 0.69	<.001
SpatialCueSelective	0.11	0.10 – 0.13	<.001
SemanticCueSpecific	0.03	0.02 – 0.04	<.001
ProbeRight	0.02	0.00 – 0.03	.009
Age	-0.03	-0.05 – -0.01	.001
TaskModularity	0.03	0.01 – 0.06	.008
RestModularity	-0.02	-0.04 – 0.01	.225
SpatialCueSelective:TaskModularity	0.02	0.00 – 0.03	.033
SpatialCueSelective:RestModularity	-0.01	-0.02 – 0.01	.226
Random Parts			
σ^2		0.042	
$\tau_{00, Subject}$		0.008	
ρ_{01}		0.865	
$N_{Subject}$		49	
$ICC_{Subject}$		0.155	
Observations		9524	
R^2 / Ω_0^2		.247 / .247	

References

1. Bullmore, E. and O. Sporns, *Complex brain networks: graph theoretical analysis of structural and functional systems.* Nat Rev Neurosci, 2009. **10**(3): p. 186-98.
2. Lancichinetti, A. and S. Fortunato, *Community detection algorithms: A comparative analysis.* Physical Review E, 2009. **80**(5).
3. Steinhaeuser, K. and N.V. Chawla, *Identifying and evaluating community structure in complex networks.* Pattern Recognition Letters, 2010. **31**(5): p. 413-421.
4. Newman, M.E., *Modularity and community structure in networks.* Proc Natl Acad Sci U S A, 2006. **103**(23): p. 8577-82.
5. Rubinov, M. and O. Sporns, *Complex network measures of brain connectivity: uses and interpretations.* Neuroimage, 2010. **52**(3): p. 1059-69.
6. Blondel, S., et al., *Fast unfolding of communities in large networks.* J Stat Mech, 2008. **P10008**: p. 6.
7. Bassett, D.S., et al., *Dynamic reconfiguration of human brain networks during learning.* PNAS, 2010. **108**(18): p. 7641-6.
8. Alavash, M., et al., *Dopaminergic modulation of hemodynamic signal variability and the functional connectome during cognitive performance.* Neuroimage, 2018. **172**: p. 341-356.
9. Alavash, M., et al., *Large-scale network dynamics of beta-band oscillations underlie auditory perceptual decision-making.* Network Neuroscience, 2017. **1**(2): p. 166-191.
10. Fortunato, S. and M. Barthelemy, *Resolution limit in community detection.* Proc Natl Acad Sci U S A, 2007. **104**(1): p. 36-41.
11. Lohse, C., et al., *Resolving structure in human brain organization: Identifying mesoscale organization in weighted network representations.* PLoS Comput Biol, 2014. **10**: p. e1003712.
12. Good, B.H., d.Y. Montjoye, and A. Clauset, *The performance of modularity maximization in practical contexts.* Phys. Rev. , 2010. **E 81**: p. 046106.
13. Betzel, R.F. and D.S. Bassett, *Multi-scale brain networks.* Neuroimage, 2016. **160**: p. 73-83.
14. Bassett, D.S., et al., *Robust detection of dynamic community structure in networks.* Chaos, 2013. **23**(1): p. 013142.
15. Sporns, O. and R.F. Betzel, *Modular brain networks.* Annu Rev Psychol, 2016. **67**: p. 613-40.
16. Lancichinetti, A. and S. Fortunato, *Consensus clustering in complex networks.* Sci Rep, 2012. **2**: p. 336.
17. Ginestet, C.E., et al., *Brain network analysis: separating cost from topology using cost-integration.* PLoS One, 2011. **6**(7): p. e21570.
18. Fornito, A., A. Zalesky, and M. Breakspear, *Graph analysis of the human connectome: promise, progress, and pitfalls.* Neuroimage, 2013. **80**: p. 426-44.
19. Bertolero, M., B. Yeo, and M. D'Esposito, *The modular and integrative functional architecture of the human brain.* PNAS, 2015. **112**: p. E6798-807.
20. Gordon, E.M., et al., *Generation and evaluation of a cortical area parcellation from resting-state correlations.* Cereb Cortex, 2016. **26**(1): p. 288-303.
21. Alavash, M., et al., *Persistency and flexibility of complex brain networks underlie dual-task interference.* Hum Brain Mapp, 2015. **36**: p. 3542-62.
22. Alavash, M., C.M. Thiel, and C. Giessing, *Dynamic coupling of complex brain networks and dual-task behavior.* Neuroimage, 2016. **129**: p. 233-46.